Advanced Composites and Hybrid Materials (2023) 6:161
https://doi.org/10.1007/s42114-023-00741-1

RESEARCH

Multifunctional flexible, crosslinked composites composed of trashed MXene sediment with high electromagnetic interference shielding performance

Sinan Zheng[1] · **Na Wu**[2] · **Yue Liu**[1] · **Qilei Wu**[3] · **Yunfei Yang**[1] · **Bin Li**[1] · **Chenxi Hu**[4] · **Jiurong Liu**[1] · **Zhihui Zeng**[1]

Received: 19 April 2023 / Revised: 10 May 2023 / Accepted: 1 September 2023 / Published online: 7 September 2023

Abstract

Developing novel nanomaterials for constructing multifunctional macrostructures in a facile, energy-efficient, sustainable, and scalable approach is urgently demanded yet remains highly challenging. Here, a type of freestanding, robust, highly flexible composite films composed of "trashed" MXene sediment (MS) are prepared in an ambient pressure casting approach. The typical green polymer of polyvinyl alcohol is employed to demonstrate the high potential of MS for constructing films with multifunctionalities, including electrically conductive, hydrophobic, photothermal, and electromagnetic interference (EMI) shielding performance. Upon the synergy of surface terminal functional groups, local defects, and numerous heterogeneous interfaces, the MS-based composites can have EMI shielding effectiveness (SE) of 76.2 dB in the X-band at the thickness of merely 590 μm and efficient SE value in the ultrabroadband frequency range of 8.2 to 40 GHz. Moreover, the EMI SE of the MS-based composites is widely controlled by adjusting the MS contents and film thickness. Combined with the sensitive and reliable photothermal performance, this work thus demonstrates a cost-effective, sustainable, and scalable strategy to prepare a type of multifunctional MS-based films with application potentials in thermal therapy, wearable electronics, electromagnetic compatible, and aerospace.

Keywords MXene sediment · Composite · Electromagnetic interference shielding · Multifunctionality · Flexible

1 Introduction

A growing number of intelligent and miniaturized electronic devices have entered human society and brought severe electromagnetic radiation or pollution [1–4]. This leads to the electromagnetic interference (EMI) or functional failure between electronic components and even has adverse influences on human health [5–7]. EMI shielding materials which can attenuate the electromagnetic waves (EMWs) are highly desired [8–11]. Conventional metal shields can hardly meet the requirement of modern EMI shields because of the drawbacks including high density, difficult processability, and easy corrosion [12, 13]. Lightweight, thin, and flexible EMI shields with excellent EMI shielding effectiveness (SE) as well as considerable mechanical strength are promising to meet the needs of current electronic devices with intelligence and portability [14–18]. As a novel type of two-dimensional (2D) materials, transition metal carbides/nitrides (MXenes) have a bright prospect in medicine [19], microbiology [20], sensing [21], energy storage [22], and catalysis [23]. Owing to the unique 2D sheet structure and rich terminal functional

---

✉ Na Wu
na.wu@org.chem.ethz.ch

✉ Jiurong Liu
jrliu@sdu.edu.cn

✉ Zhihui Zeng
zhihui.zeng@sdu.edu.cn

[1] Key Laboratory for Liquid–Solid Structural Evolution and Processing of Materials, Ministry of Education and School of Materials Science and Engineering, Shandong University, Jinan, People's Republic of China

[2] Department of Chemistry and Applied Biosciences, ETH Zurich, CH-8093 Zurich, Switzerland

[3] Science and Technology on Electromagnetic Compatibility Laboratory, China Ship Development and Design Centre, Wuhan, People's Republic of China

[4] College of Science, Civil Aviation University of China, Tianjin, People's Republic of China

groups, MXenes exhibit excellent electrical conductivity and diverse surface characteristics [24–26], which is conductive to the EMI shielding applications [27, 28]. For example, Shahzad et al. prepared the flexible, robust MXene films by vacuum filtration [29], which showed EMI SE of 90 dB at the thickness of tens of microns. Liu et al. employed a hydrazine-induced foaming process to fabricate free-standing, flexible MXene foams with good EMI shielding properties [30]. These reports demonstrate the great application potential of MXenes for high-performance EMI shielding materials in portable and wearable electronic devices [31–33].

Currently, researchers are mainly focusing on the preparation of single-layer or few-layer MXenes for constructing high-performance EMI shields. However, low yield of these MXene nanosheets from the MAX precursors as well as the poor oxidation stability in the O_2/H_2O environment exists, restricting the applications [34–36]. In the liquid phase preparation process of MXenes, few MAX precursors can be efficiently exfoliated into the single-layer or few-layer MXenes [37], and the rest comes in the form of by-products named MXene sediment (MS). The dominant MS, consisting of unetched highly conductive MAX, multilayer MXene, and a small amount of single-layer or few-layer MXene, is usually discarded directly [38–40]. This undoubtedly causes the waste of resources and energy and greatly increases the cost of MXene-based functional or EMI shielding materials [41]. Considering the great demand for new EMI shielding materials in the current society, exploring the MS for constructing the EMI shielding monoliths is highly promising yet remains rarely reported. It can be ascribed to that the poor interfacial interactions between the MS particles give the challenge for preparing robust, durable, freestanding MS-based EMI shielding macrostructures. Fortunately, we have ascertained that, like MXenes [42], there are numerous hydrophilic terminal groups such as –OH, =O, and –F on the surface of MS. The good hydrophilicity allows for the embedment of hydrophilic polymers, showing excellent gelation capability or interfacial interactions, which is beneficial for fabricating the robust composites with good conductivity [43–45]. Therefore, a high EMI shielding performance of composites composed of the “trashed” MS is highly anticipated. Moreover, functionalities for the EMI shields are highly demanded due to the emerging development of the Internet of Things (IoT) and next-generation electronics, which proposed the exploration of the multifunctional MS-based composites.

Here, the commonly employed polyvinyl alcohol (PVA) as a green polymer that is inexpensive, non-toxic, and biocompatible [46, 47] is a typical example for assisting in the preparation of freestanding yet robust MS-based films in a facile, scalable ambient-pressure-dried approach. Abundant hydroxyl functional groups of PVA not only induce strong hydrogen bonds with the hydrophilic groups of MS [48–50], but also render the further chemical crosslinking treatment of the MS-based composites. This leads to the excellent mechanical strength and flexibility, good hydrophobicity, and water resistance of the MS-based composites. The PVA or MS content is facilely adjusted in a wide range of 10 to 70 wt%, inducing the wide-ranging controllability of the EMI SE of MS-based composites. The EMI SE of MS-based films can reach 29.9 to 84.8 dB at a thickness of 0.12 to 0.59 mm, respectively. In addition to the EMI shielding stability of the MS-based composites upon mechanical deformations, an efficient EMI SE in the ultra-broadband frequency range of 8.2 to 40 GHz is achieved. Combined with the high photothermal performance, this work thus suggests a new avenue for facile, scalable manufacturing of thin, flexible, and multifunctional MS-based composites composed of “trashed” MXene for applications in EMI compatibility, smart heaters, next-generation electronics, and aerospace.

2 Experimental section

2.1 Materials

Lithium fluoride (LiF) and polyvinyl alcohol (PVA) were purchased from Aladdin; hydrochloric acid (HCl, 6M) was purchased from Sinopharm Chemical Reagent Co., Ltd.; Ti_3AlC_2 (MAX) was provided by Laizhou Kai Kai Ceramic Materials Co., Ltd.; and poly ((phenyl isocyanate)-co-formaldehyde) (PMDI) and acetonitrile were purchased from Macklin.

2.2 Composite preparation

2.2.1 Preparation of MS

The MS was obtained as a by-product in the preparation of MXene nanosheets. Briefly, 3.2 g LiF was slowly added to 40 mL of 6 M HCl at room temperature with vigorous stirring. After LiF was completely dissolved, 2.0 g Ti_3AlC_2 MAX was added to the above solution to react at 35 ℃ for 24 h. Then, the product was centrifuged at 3500 rpm and washed to pH≈6. The suspension was violently shaken for 30 min and re-centrifuged to separate the supernatant Ti_3C_2 MXene nanosheet dispersion. After collecting the upper Ti_3C_2 MXene aqueous dispersion for other uses, the remaining centrifugally MS particles were collected without adding any additional additives.

2.2.2 Fabrication of MS-based composite film

The freestanding MS-based composite films with various MS contents and thicknesses were prepared by ambient pressure casting method. Unlike vacuum-assisted filtering, which necessitates high vacuum conditions and costly equipment, ambient pressure drying is less reliant on the equipment systems and offers greater process optimization flexibility, allowing for greater cost savings. First, the prepared MS suspension with a concentration of 15 wt% was mixed with 5 wt% PVA solution by magnetic stirring for 3 h. Then, the mixture was cast into a Teflon mold and dried in an oven at 50 ℃ to obtain the freestanding, flexible PVA/MS composite films. The MS content was controlled by adjusting the ratio of MS to PVA in the mixture, and the thickness of the composite was controlled by changing the amount of the mixture. In addition, the PVA/MS composite films with abundant hydroxyl groups could be easily chemically crosslinked by poly ((phenyl isocyanate)-co-formaldehyde) (PMDI) as crosslinking agent for designed hydrophobicity. Herein, PMDI was dissolved in a mixture of acetonitrile/methyl caproate (4:1, volume ratio) at a volume ratio of 1:9, and PVA/MS composite films were immersed in the above solution for a reaction at 70 ℃ for 2 h. Finally, C-PVA/MS composite films were obtained by washing with acetone and drying at room temperature.

2.3 Characterization

The morphology and microstructure were characterized via a high-resolution transmission electron microscopy (HR-TEM; JEOL JEM-2100) and a field-emission scanning electron microscopy (FE-SEM; Hitachi SU-70). The crystal structures and chemical composition were evaluated by an X-ray diffraction (XRD; Rigaku D/Max-kA) and an X-ray photoelectron spectroscopy (XPS; Thermo ESCALAB 250XI), respectively. The tensile properties were measured by a microcomputer-controlled electronic universal testing machine (Fangyuan; i5-200N), and the corresponding Young's modulus was calculated from the slope of the linear region of the stress-strain curves. The electrical conductivity was carried out by 4-terminal measurements (Tonghui test system; TH26011CS). The light source for the photothermal test was provided by a xenon lamp (Merry Change; MC-PF300-UV) with controllable power densities. The infrared radiation (IR) thermal images were taken by an IR thermal camera (Fotric; FLIR E8xt). The surface temperature of the samples was measured by a digital thermometer (UNI-T; UT325) with its T-type thermocouple contacting the surface of the sample.

The EMI SE was measured via the waveguide method by a vector network analyzer (VNA, Agilent PNA N5244A). The as-prepared samples were cut into the desired sizes of 22.86 mm × 10.16 mm, 15.8 mm × 7.9 mm, 10.7 mm × 4.3 mm, and 7.1 mm × 3.6 mm in the frequency range of X-band (8.2–12.4 GHz), Ku-band (12.4–18 GHz), K-band (18–26.5 GHz), and Ka-band (26.5–40 GHz), respectively. More than five samples were performed for each component under the same testing condition. The total SE (SE_T), shielding by reflection (SE_R), and shielding by absorption ($\mathrm{SE_A}$) can be calculated through the S-parameter as follows.

$$SE_T = -10\log\left(\left|S_{12}\right|^2\right) = -10\log\left(\left|S_{21}\right|^2\right) \tag{1}$$

$$SE_R = -10\log\left(1-\left|S_{11}\right|^2\right) \tag{2}$$

$$SE_A = -10\log\left(\frac{\left|S_{12}\right|^2}{1-\left|S_{11}\right|^2}\right) = SE_T - SE_R \tag{3}$$

3 Results and discussion

Prior to fabricating the PVA/MS flexible composite films, the MS is prepared (Fig. 1a). The coexistence of multi-layer MXene and unetched MAX in MS can be observed from the SEM and TEM images in Fig. 1b–d. Atoms in the delaminated MXene nanosheets exhibit hexagonal stacking, as shown in Fig. 1c. The AFM image further confirms that the MS contained the multi-layer MXene and delaminated MXene nanosheets (Fig. 1e). Through the simple, scalable casting approach, the MS-based composite films that can bend, roll, or even twist are prepared, exhibiting a great potential for flexible devices (Fig. 1f). The cross-sectional SEM image of PVA/MS composite films and the EDS mappings further show the uniform distribution of MS in the composites (Fig. 1g, h), which is beneficial for generating an effective MS-based conductive network. Furthermore, numerous hydroxyl functional groups of the PVA promote the efficient chemical cross-linking with PMDI, introducing the hydrophobic skeleton of PMDI and thus endowing the PVA/MS composite films with designed hydrophobicity (Fig. 1i). Moreover, the formed covalent bonds in the chemical crosslinking process improved the stability of the MS-based composites, and thus the crosslinked PVA/MS (C-PVA/MS) composite films remain intact after soaking in water for 24 h, in contrast to the obvious delamination of the MS/PVA films without crosslinking (Fig. 1j).

The structure and properties of PVA/MS composite films were further characterized. The XRD patterns in Fig. 2a showcase the successful preparation of PVA/MS composites. Furthermore, the peak at 7.198° can be attributed to the (002) plane with a 1.246 nm interplanar spacing of MXenes [51, 52]. The diffraction peaks at 9.5°, 19.2°, 34.1°, 39.0°, and 41.8° are indexed to (002), (004), (101), (104) and (105) planes of Ti_3AlC_2 MAX (JCPDS 52-0875), respectively [53], showing the existence of unetched MAX in MS (Fig. S1). By comparing the Ti 2p XPS spectra of MS and MXene, it can be found that the chemical bonds of Ti 2p in MS and MXene are similar, where the characteristic peaks of Ti-C, Ti^{2+}, and Ti^{3+} are consistent with the previously reported MXenes

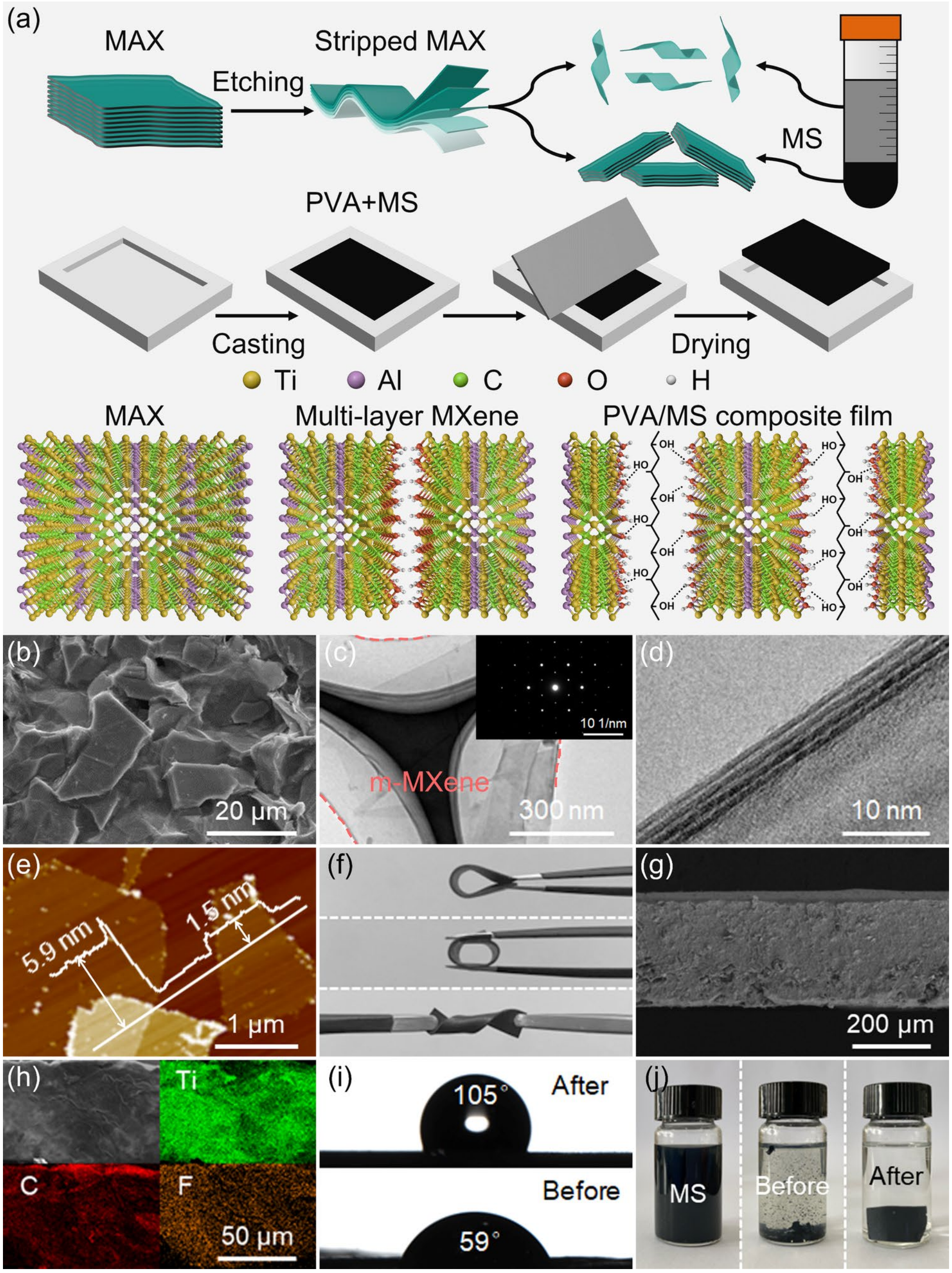

Fig. 1 **a** The schematic for the fabrication process of PVA/MS composite films. The **b** SEM image, **c** and **d** TEM image (the inset is SAED pattern), and **e** AFM image of MS. **f** The digital photograph of the MS-based composite films showing flexibility including bendability, rollability, and twistability. The **g** cross-sectional SEM image, and **h** elemental mappings of free-standing MS-based composite films. **i** The water contact angles of the C-PVA/MS (upside) and PVA/MS (downside) composite films. **j** The digital photograph of the MS (left), PVA/MS film (middle), and C-PVA/MS films (right) after soaking in water for 24 h

(Fig. S2) [54]. Compared with MS, the enhanced C 1s and O 1s in PVA/MS composite films efficiently prove the compounding of PVA as a polymer binder with MS. The addition of N element and C=O bond demonstrates the chemical crosslinking process of the C-PVA/MS composites (Figs. 2b, c, S3). Here, the reactions between PMDI, PVA, and MS lead to the formation of strong covalent interactions and introduce hydrophobic benzene ring of PMDI, which is instrumental in improving the water resistance, stability, and durability.

The tensile curves of PVA/MS composite films reveal that the tensile strength (σ) and elongation at break (ε) increase with increasing PVA content (Fig. 2d). The ε of the composite films containing 70 wt% PVA can reach 56%, showing a good plastic deformation ability. Figure 2e shows that the increased PVA content increases the tensile strength despite that too much PVA results in decreased Young's modulus of composite. Compared with that the MS cannot form freestanding films due to the poor gelation capability, the PVA/MS composite films exhibit good mechanical properties, suggesting the vital role of PVA as an efficient binder in preparing freestanding, robust MS-based films. It should be noted that the addition of PVA also affects the conductivity and density of composite films. When the PVA

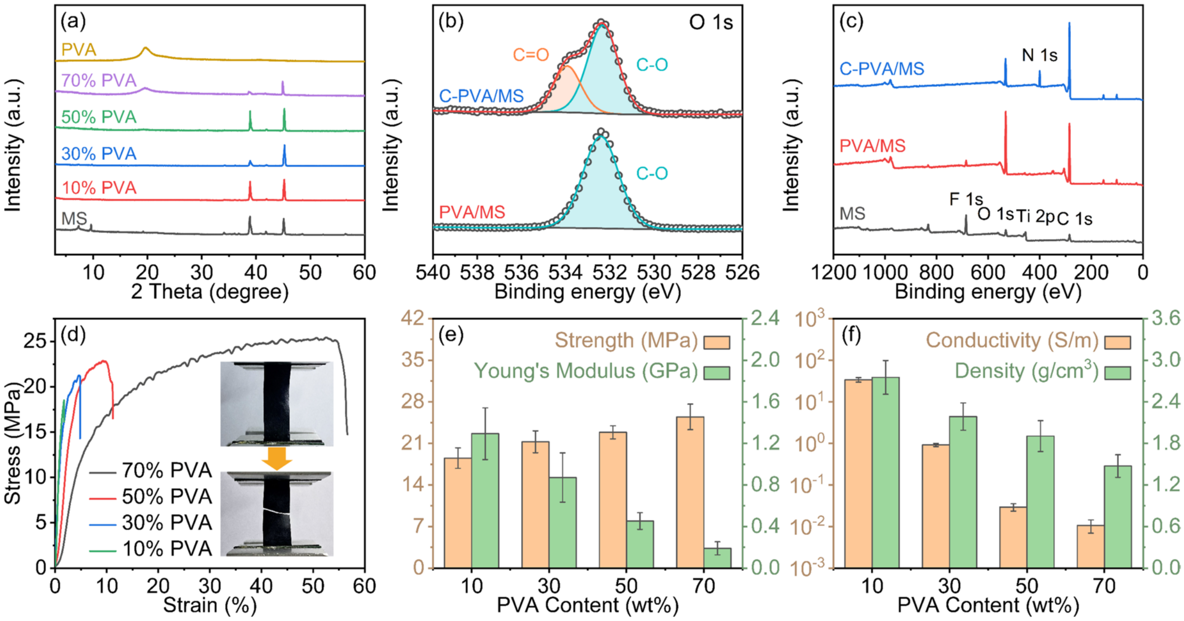

Fig. 2 The structure and properties of MS-based composite films. **a** The XRD pattern of MS, PVA, and PVA/MS composite films with various PVA contents. **b** The O 1s XPS spectra of the PVA/MS and C-PVA/MS. **c** The survey scan XPS spectra of MS, PVA/MS, and C-PVA/MS. The **d** stress-strain curves, **e** corresponding tensile strength and Young's modulus, and **f** conductivity and density of MS-based composite films with various PVA contents

content increases from 10 to 70 wt% for the composites, the conductivity and density decrease from 33.9 to 0.01 S/m and 2.75 to 1.47 g/cm^3, respectively (Fig. 2f). In summary, the controllable PVA content renders the MS-based films the potential for adjusting and optimizing the properties.

EMI SE of MS-based films with various PVA contents and thicknesses in the X-band frequency range are obtained. At a thickness of merely 118 μm (Fig. 3a), the EMI SE of the composite films containing 10 wt% PVA can reach 30.8 dB, and that of the composite films containing 30 wt% PVA can also reach 22.4 dB, which meets the SE requirements of 20 dB for the commercial EMI shields [55, 56]. Generally, the EMI shielding performance of materials comes from the synergy between absorption and reflection of EMWs, which are correlated with the electric dipoles and mobile charge carriers, respectively [57, 58]. Here, SE_A and SE_R values of PVA/MS composite films were calculated to further clarify the EMI shielding mechanism. As displayed in Fig. 3b, at the same thickness, SE_A and SE_R values of composite films decrease with increased PVA content. More MS conduces to the more contacts between MS and the formation of conductive paths for the MS-based composite films, resulting in higher conductivity and SE_R values [59]. Meanwhile, the mismatch of conductivity between PVA and MS contributes to high interfacial polarization under the electric field of incident EMWs, which can improve the SE_A of composites [60]. Moreover, electric dipoles resulting from abundant terminal functional groups in MS can generate dipole polarization in the alternating electric field, further improving the SE_A [61]. Therefore, the decreased MS content leads to the weakened absorption and reflection losses of incident EMWs, and thus, the SE_T is decreased.

Here, the power coefficient is also employed to show the shielding process [62], where *R*, *A*, and *T* represent the reflection, absorption, and transmission power coefficients, respectively. As shown in Fig. 3c, when the composite films contain a low PVA content, more than 80% of EMWs are reflected, and about 15% of EMWs enter the composite films and are almost completely absorbed. When the PVA content gradually increases, better impedance matching makes for the obviously reduced reflection of EMWs, but the absorption of EMWs is obviously increased. When the thickness increases to 230 μm, the EMI SE values of PVA/MS composite films containing 10 wt%, 30 wt%, and 50 wt% PVA increase to 40.9, 27.9, and 18.5 dB, respectively (Fig. 3d). A similar variation trend of SE_A and SE_R values of composite films is displayed at different thicknesses (Fig. 3e), and the reflection of EMWs is still dominant (Fig. 3f).

The composite films with the same PVA content have higher EMI SE at a higher thickness (Fig. 3g–i). When the thickness of the MS-based films containing 10 wt% PVA increases from 118 to 590 μm, the EMI SE increases from 30.8 to 76.2 dB. And the EMI SE of composites can reach 84.8 dB at the thickness of merely 590 μm (Fig. 3g). When surpassing the commercial SE value, the thicknesses of composite films containing 30 wt% and 50 wt% PVA are

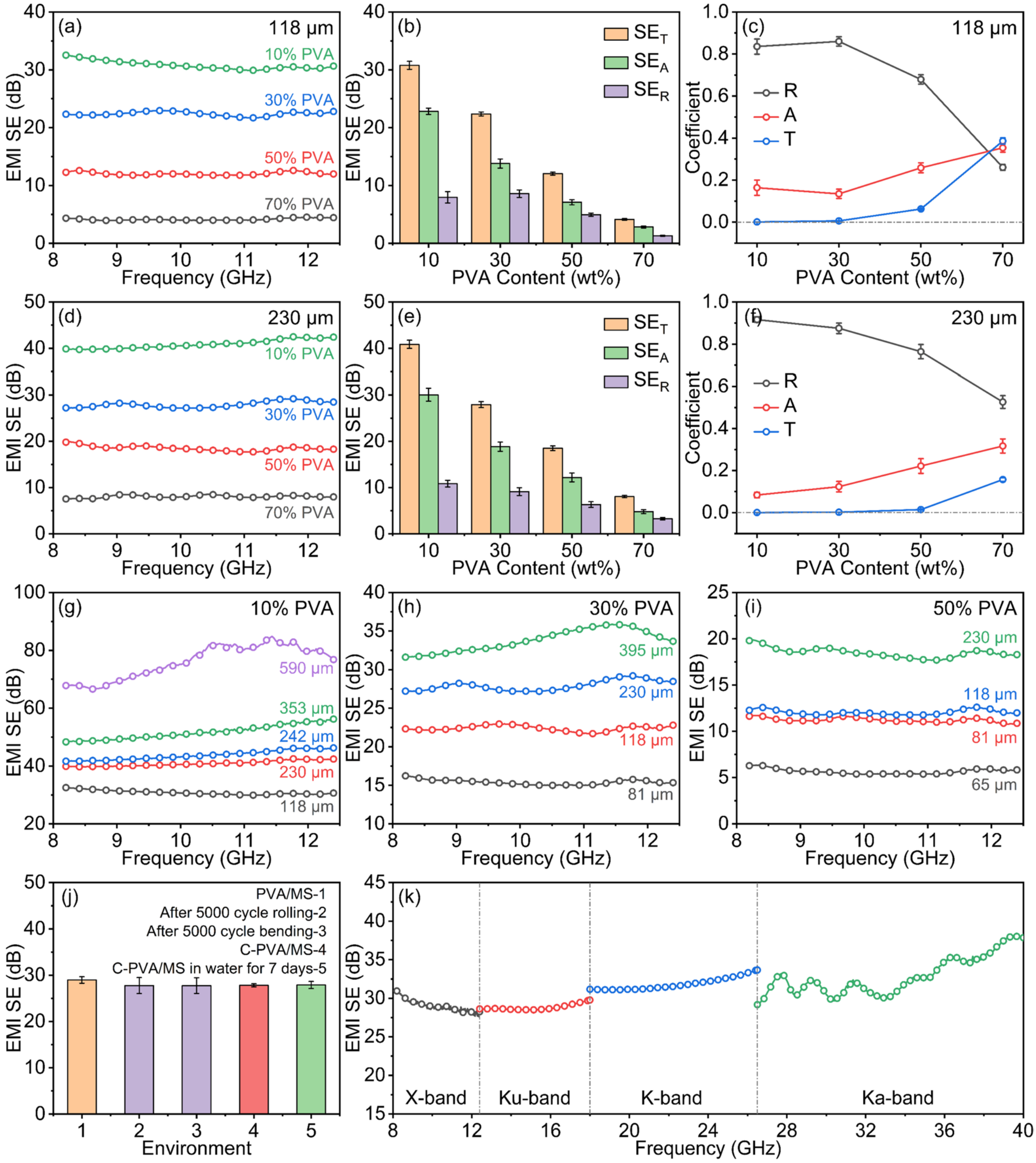

Fig. 3 The EMI shielding performance of MS-based composite films. The **a** EMI SE in X-band; **b** corresponding SE_T, SE_A, and SE_R values; and **c** power coefficients of MS-based composite films with various PVA contents at 118 μm. The **d** EMI SE in X-band; **e** corresponding SE_T, SE_A, and SE_R values; and **f** power coefficients of MS-based composite films with various PVA contents at 230 μm. The EMI SE in X-band of PVA/MS composite films with various thicknesses and **g** 10 wt%, **h** 30 wt%, and **i** 50 wt% PVA contents. **j** The EMI SE in X-band of MS-based composite films (10 wt% PVA, 118 μm) after 5000-cycle rolling and bending, and C-PVA/MS after soaking in water for 7 days. **k** The EMI SE in an ultra-broadband frequency range for the MS-based composite films with 10 wt% PVA at a thickness of 118 μm

only around 118 and 230 μm, respectively. The EMI shielding performance is superior to most polymer composites embedded with various nanofillers (Table S1), such as carbon nanotube (CNT)/polyurethane composite films showing an SE of 35 dB at a thickness of 2.3 mm [33], reduced graphene oxide (rGO)/PS films showing SE of 45.1 dB at a thickness of 2.5 mm [63], or MXene/PVDF films showing SE of 48.8 dB at a thickness of 2.0 mm [64]. The addition of PVA not only makes MS form freestanding, flexible films with high EMI SE, but also endows the composites with stale EMI shielding performance. For instance, the MS-based composite films can maintain similar EMI SE

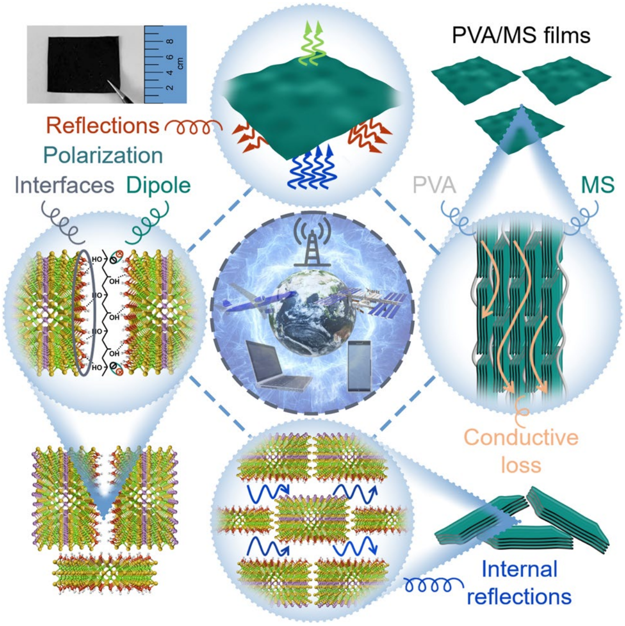

Fig. 4 The schematic illustration of EMI shielding mechanism for MS-based composite films

values after 5000 times of rolling and bending treatment, convincingly demonstrating the durability for flexible electronics. The chemical crosslinking of composites slightly affects the EMI shielding performance (Fig. 3j), and thus, the crosslinked MS-based films have good hydrophobicity and stable EMI SE even after the immersion in water for 7 days. This is of vital importance for some special application scenarios with a high humidity condition. Moreover, even in an ultra-broadband frequency range, including typical X (8.2–12.4 GHz), Ku (12.4–18GHz), K (18–26.5GHz), and Ka (26.5–40GHz) bands, efficient EMI SE values can be achieved (Fig. 3k), showing the great application potential of the MS-based composites.

Based on the analysis, we propose the EMI shielding mechanism of MS-based composite films as shown in Fig. 4. When EMW is incident on the surface of the films, a part of EMW is immediately reflected into the atmosphere due to the impedance mismatch [65], and the rest penetrates into the composites. The incident EMW undergoes conduction loss through the electron migration paths generated by MS lapping [66], as well as polarization loss through electric dipoles caused by terminal functional groups and local defects of the MS. Besides, high interfacial polarization caused by conductivity mismatch in the PVA/MS interfaces boosts the polarization loss capability of composites [67, 68]. Furthermore, the layered structure of MS is also instrumental in the multiple reflections of incident EMW, extending the propagation path and increasing the interactions between EMW and MS [69]. The coordination and synergy of MS and PVA jointly contribute to the excellent EMI shielding performance of the MS-based composite films.

Apart from hydrophobicity, conductivity, and EMI shielding performance, the flexible MS-based composite films are of great value for exploring more functionalities. Here, the remarkable photothermal response properties of PVA/MS composite films were accomplished. Figure 5a shows that the temperature of MS-based composite film rises rapidly under a xenon lamp irradiation and reaches equilibrium, and the equilibrium temperature increases with increased light power density. The equilibrium temperatures of films containing 10 wt% PVA at power densities of 50, 100, 150, 200, and 250 mW/cm^2 were 41.1, 56.5, 74.0, 95.4, and 111.3 ℃, respectively. In addition, the MS-based films containing different PVA mass ratios have different equilibrium temperatures at the same light power density. For instance, at a power density of 200 mW/cm^2, the equilibrium temperatures of composite films containing 70, 50, 30, and 10 wt% PVA reach 46.4, 53.6, 72.3, and 95.4 ℃, respectively (Fig. 5b). At a constant power density value, the photothermal curves of the composite films in the first and tenth cycles are similar, showing the stable and repeatable photothermal performance (Fig. 5c). We also tested the photothermal stability of MS-based composite films during multiple cycles at various light power densities of 100, 150, and 250 mW/cm^2, respectively. As shown in Fig. 5d, the composite films exhibit the regular ascending and descending temperature cycles when the light turns on and off, respectively, and the equilibrium temperature is stable at a fixed light power density. Figure 5e shows that MS-based films have a uniform surface temperature distribution, and the composite films can maintain a stable temperature for a long time, showing the reliability. Therefore, the equilibrium temperature of composite films is positively correlated with MS content and light power density (Fig. 5f), which can be ascribed to the strong light absorption ability and local surface plasmon resonance characteristics of MS as MXenes do [70–75]. This contributes to the easy controllability of photothermal performance of the MS-based films. Sensitive and stable photothermal response to various light power densities (Fig. 5g) enables the MS-based films to be highly potential in many application scenarios, such as photothermal therapy and smart wearable heaters or displays.

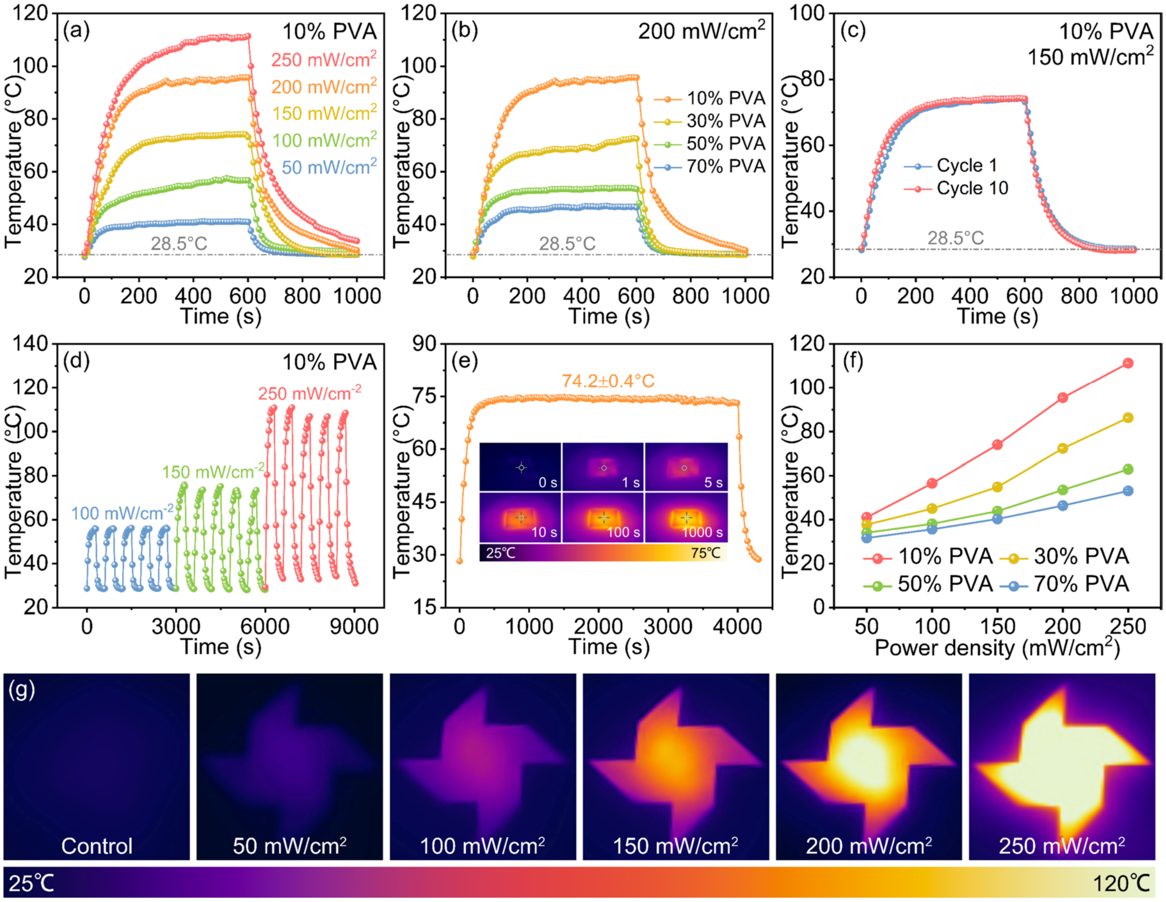

Fig. 5 The photothermal curves of MS-based composite films **a** with 10 wt% PVA at various light power densities, **b** with various PVA contents at the 200 mW/cm^2 power density, **c** with 10 wt% PVA content at the 150 mW/cm^2 power density under the first and tenth heating/cooling cycles, and **d** with 10 wt% PVA at various power densities under heating/cooling cycles. **e** The stability test of composite films with 10 wt% PVA at the 150 mW/cm^2 power density (inset shows the infrared thermal images). **f** The equilibrium temperature versus input power density curves of composite films with various PVA contents. **g** The infrared images of surface temperature of composite films with 10 wt% PVA under various light power densities

4 Conclusion

A type of freestanding, robust, highly flexible MS-based composite films composed of trashed MXene sediment are fabricated using a simple, facile, and scalable ambient pressure casting approach. The addition of PVA not only stabilizes the structure of MS-based macrostructures, but also contributes to the excellent mechanical strength and flexibility, including bendability, rollability, and twistability. Benefiting from the synergy of surface terminal functional groups, local defects, and numerous MS-PVA interfaces, the MS-based films exhibit excellent EMI shielding performance. The films containing 10 wt% PVA show an EMI SE of 30.8 to 76.2 dB in the X-band at a thickness of 118 to 590 μm, respectively, and an SE of more than 20 dB in the ultra-broadband of 8.2 to 40 GHz at a low thickness. Moreover, the EMI SE of MS-based films is widely and easily controlled by adjusting the PVA/MS contents and film thickness, exhibiting the controllable EMI shielding performance. In addition, the MS-based films show sensitive and reliable photothermal response, indicating the bright prospects in portable electronics and smart wearable heaters. The preparation of the freestanding, robust, and highly flexible MS-based films composed of the trashed MXene sediment is scalable, sustainable, and waste-free. Combined with the multifunctionalities involving hydrophobicity, electrical conduction, and photothermal and EMI shielding performance, the MS-based films exhibit the great application potential for next-generation flexible electronics.

Supplementary Information The online version contains supplementary material available at https://doi.org/10.1007/s42114-023-00741-1.

Acknowledgements The authors acknowledge the assistance of Shandong University Testing and Manufacturing Center for Advanced Materials.

Author contribution Sinan Zheng: conceptualization, formal analysis, writing—original draft. Na Wu: investigation. Yue Liu: methodology. Qilei Wu: resources. Yunfei Yang: software. Bin Li: validation. Chenxi Hu: supervision. Jiurong Liu: project administration. Zhihui Zeng: writing—review and editing.

Funding This work was financially supported by the National Key R&D Program of China (No. 2021YFB3502500), National Natural Science Foundation of China (No. 22205131), Natural Science Foundation of Shandong Province (No. 2022HYYQ-014), Provincial Key Research and Development Program of Shandong (No. 2019JZZY010312, 2021ZLGX01), New 20 Funded Programs for Universities of Jinan (No. 2021GXRC036), and the Qilu Young Scholar Program of Shandong University (No. 31370082163127).

Declarations

Competing interests The authors declare no competing interests.

References

1. Cao MS, Cao YZ, He P, Shu JC, Cao WQ, Yuan J (2019) 2D MXenes: electromagnetic property for microwave absorption and electromagnetic interference shielding. Chem Eng J 359:1265–1302. https://doi.org/10.1016/j.cej.2018.11.051
2. Wan HJ, Liu N, Tang J, Wen QY, Xiao X (2021) Substrate-independent $Ti_3C_2T_x$ MXene waterborne paint for terahertz absorption and shielding. ACS Nano 15:13646–13652. https://doi.org/10.1021/acsnano.1c04656
3. Cao WT, Ma C, Tan S, Ma MG, Wan PB, Chen F (2019) Ultrathin and flexible CNTs/MXene/cellulose nanofibrils composite paper for electromagnetic interference shielding. Nano-Micro Lett 11:72. https://doi.org/10.1007/s40820-019-0304-y
4. Jiang DW, Murugadoss V, Wang Y, Lin J, Ding T, Wang ZC, Shao Q, Wang QC, Liu H, Lu N, Wei RB, Subramania A, Guo ZH (2019) Electromagnetic interference shielding polymers and nanocomposites-a review. Polym Rev 59:280–337. https://doi.org/10.1080/15583724.2018.1546737
5. Yao JR, Zhang L, Yang F, Jiao ZB, Tao XW, Yao ZJ, Zheng YM, Zhou JT (2022) Superhydrophobic $Ti_3C_2T_x$ MXene/aramid nanofiber films for high-performance electromagnetic interference shielding in thermal environment. Chem Eng J 446:136945. https://doi.org/10.1016/j.cej.2022.136945
6. Cao WT, Chen FF, Zhu YJ, Zhang YG, Jiang YY, Ma MG, Chen F (2018) Binary strengthening and toughening of MXene/cellulose nanofiber composite paper with nacre-inspired structure and superior electromagnetic interference shielding properties. ACS Nano 12:4583–4593. https://doi.org/10.1021/acsnano.8b00997
7. Wu XY, Tu TX, Dai Y, Tang PP, Zhang Y, Deng ZM, Li LL, Zhang HB, Yu ZZ (2021) Direct ink writing of highly conductive MXene frames for tunable electromagnetic interference shielding and electromagnetic wave-induced thermochromism. Nano-Micro Lett 13:148. https://doi.org/10.1007/s40820-021-00665-9
8. Lee S, Jo I, Kang S, Jang B, Moon J, Park JB, Lee S, Rho S, Kim Y, Hong BH (2017) Smart contact lenses with graphene coating for electromagnetic interference shielding and dehydration protection. ACS Nano 11:5318–5324. https://doi.org/10.1021/acsnano.7b00370
9. Luo JC, Wang L, Huang XW, Li B, Guo Z, Song X, Lin LW, Tang LC, Xue HG, Gao JF (2019) Mechanically durable, highly conductive, and anticorrosive composite fabrics with excellent self-cleaning performance for high-efficiency electromagnetic interference shielding. ACS Appl Mater Interfaces 11:10883–10894. https://doi.org/10.1021/acsami.8b22212
10. Huang L, Li JJ, Li YB, Heb XD, Yuan Y (2019) Lightweight and flexible hybrid film based on delicate design of electrospun nanofibers for high-performance electromagnetic interference shielding. Nanoscale 11:8616–8625. https://doi.org/10.1039/C9NR02102G
11. Xie PT, Liu Y, Feng M, Niu M, Liu CZ, Wu NN, Sui KY, Patil RR, Pan D, Guo ZH, Fan RH (2021) Hierarchically porous Co/C nanocomposites for ultralight high-performance microwave absorption. Adv Compos Hybrid Ma 4:173–185. https://doi.org/10.1007/s42114-020-00202-z
12. Yu JW, Gu WH, Zhao HQ, Ji GB (2021) Lightweight, flexible and freestanding PVA/PEDOT: PSS/Ag NWs film for high-performance electromagnetic interference shielding. Sci China Mater 64:1723–1732. https://doi.org/10.1007/s40843-020-1557-3
13. Gargama H, Thakur AK, Chaturvedi SK (2015) Polyvinylidene fluoride/nickel composite materials for charge storing, electromagnetic interference absorption, and shielding applications. J Appl Phys 117:224903. https://doi.org/10.1063/1.4922411
14. Wei QW, Pei SF, Qian XT, Liu HP, Liu ZB, Zhang WM, Zhou TY, Zhang ZC, Zhang XF, Cheng HM, Ren WC (2020) Superhigh electromagnetic interference shielding of ultrathin aligned pristine graphene nanosheets film. Adv Mater 32:1907411. https://doi.org/10.1002/adma.201907411
15. Song WL, Guan XT, Fan LZ, Cao WQ, Wang CY, Zhao QL, Cao MS (2015) Magnetic and conductive graphene papers toward thin layers of effective electromagnetic shielding. J Mater Chem A 3:2097–2107. https://doi.org/10.1039/C4TA05939E
16. Shen B, Zhai WT, Tao MM, Ling JQ, Zheng WG (2013) Lightweight, multifunctional polyetherimide/graphene@Fe_3O_4 composite foams for shielding of electromagnetic pollution. ACS Appl Mater Interfaces 5:11383–11391. https://doi.org/10.1021/am4036527
17. Zhang Z, Liu MX, Ibrahim MM, Wu HK, Wu Y, Li Y, Mersal GAM, El Azab IH, El-Bahy SM, Huang MN, Jiang YX, Liang GM, Xie PT, Liu CZ (2022) Flexible polystyrene/graphene composites with epsilon-near-zero properties. Adv Compos Hybrid Ma 5:1054–1066. https://doi.org/10.1007/s42114-022-00486-3
18. Liu MX, Wu HK, Yan Wu, Xie PT, Pashameah RA, Abo-Dief HM, El-Bahy SM, Wei YL, Li GX, Li WT, Liang GM, Liu CZ, Sun K, Fan RH (2022) The weakly negative permittivity with low-frequency-dispersion behavior in percolative carbon nanotubes/epoxy nanocomposites at radio-frequency range. Adv Compos Hybrid Ma 5:2021–2030. https://doi.org/10.1007/s42114-022-00541-z
19. Shamsabadi AA, Gh MS, Anasori B, Soroush M (2018) Antimicrobial mode-of-action of colloidal $Ti_3C_2T_X$ MXene nanosheets. ACS Sustain Chem Eng 6:16586–16596. https://doi.org/10.1021/acssuschemeng.8b03823
20. Liu GY, Zou JH, Tang QY, Yang XY, Zhang YW, Zhang Q, Huang W, Chen P, Shao JJ, Dong XC (2017) Surface modified Ti_3C_2 MXene nanosheets for tumor targeting photothermal/photodynamic/chemo synergistic therapy. ACS Appl Mater Interfaces 9:40077–40086. https://doi.org/10.1021/acsami.7b13421
21. Yang ZJ, Jiang L, Wang J, Liu FM, He JM, Liu A, Lv SY, You R, Yan X, Sun P, Wang CG, Duan Y, Lu GY (2021) Flexible resistive NO_2 gas sensor of three-dimensional crumpled MXene $Ti_3C_2T_x$/ZnO spheres for room temperature application. Sens Actuators B Chem 326:128828. https://doi.org/10.1016/j.snb.2020.128828
22. Wang XF, Kajiyama S, Iinuma H, Hosono E, Oro S, Moriguchi I, Okubo M, Yamada A (2015) Pseudocapacitance of MXene nanosheets for high-power sodium-ion hybrid capacitors. Nat Commun 6:6544. https://doi.org/10.1038/ncomms7544
23. Seh ZW, Fredrickson KD, Anasori B, Kibsgaard J, Strickler AL, Lukatskaya MR, Gogotsi Y, Jaramillo TF, Vojvodic A (2016) Two-dimensional molybdenum carbide (MXene) as an efficient

electrocatalyst for hydrogen evolution. ACS Energy Lett 1:589–594. https://doi.org/10.1021/acsenergylett.6b00247

24. Li XL, Yin XW, Liang S, Li MH, Cheng LF, Zhang LT (2019) 2D carbide MXene Ti_2CT_X as a novel high-performance electromagnetic interference shielding material. Carbon 146:210–217. https://doi.org/10.1016/j.carbon.2019.02.003
25. Wang XY, Liao SY, Wan YJ, Huang HP, Li XM, Hu YG, Zhu PL, Sun R, Wong CP (2022) Near-field and far-field EMI shielding response of lightweight and flexible MXene-decorated polyester textiles. Mater Today Phys 23:100644. https://doi.org/10.1016/j.mtphys.2022.100644
26. Feng SY, Zhan ZY, Yi Y, Zhou ZH, Lu CH (2022) Facile fabrication of MXene/cellulose fiber composite film with homogeneous and aligned structure via wet co-milling for enhancing electromagnetic interference shielding performance. Compos Part A Appl Sci Manuf 157:106907. https://doi.org/10.1016/j.compositesa.2022.106907
27. Zhang SL, Huang PF, Wang JL, Zhuang ZH, Zhang Z, Han WQ (2020) Fast and universal solution-phase flocculation strategy for scalable synthesis of various few-layered MXene powders. J Phys Chem Lett 11:1247–1254. https://doi.org/10.1021/acs.jpclett.9b03682
28. Wu LM, You Q, Shan YX, Gan SW, Zhao YT, Dai XY, Xiang YJ (2018) Few-layer $Ti_3C_2T_x$ MXene: a promising surface plasmon resonance biosensing material to enhance the sensitivity. Sens Actuators B Chem 277:210–215. https://doi.org/10.1016/j.snb.2018.08.154
29. Shahzad F, Alhabeb M, Hatter CB, Anasori B, Hong SM, Koo CM, Gogotsi Y (2016) Electromagnetic interference shielding with 2D transition metal carbides (MXenes). Science 353:1137–1140. https://doi.org/10.1126/science.aag2421
30. Liu J, Zhang HB, Sun RH, Liu YF, Liu ZS, Zhou AG, Yu ZZ (2017) Hydrophobic, flexible, and lightweight MXene foams for high-performance electromagnetic-interference shielding. Adv Mater 29:1702367. https://doi.org/10.1002/adma.201702367
31. Luo JC, Gao SJ, Luo H, Wang L, Huang XW, Guo Z, Lai XJ, Lin LW, Li RKY, Gao JF (2021) Superhydrophobic and breathable smart MXene-based textile for multifunctional wearable sensing electronics. Chem Eng J 406:126898. https://doi.org/10.1016/j.cej.2020.126898
32. Chen Y, Zhang HB, Yang YB, Wang M, Cao AY, Yu ZZ (2016) High-performance epoxy nanocomposites reinforced with three-dimensional carbon nanotube sponge for electromagnetic interference shielding. Adv Funct Mater 26:447–455. https://doi.org/10.1002/adfm.201503782
33. Zeng ZH, Jin H, Chen MJ, Li WW, Zhou LC, Zhang Z (2016) Lightweight and anisotropic porous MWCNT/WPU composites for ultrahigh performance electromagnetic interference shielding. Adv Funct Mater 26:303–310. https://doi.org/10.1002/adfm.201503579
34. Wu XY, Han BY, Zhang HB, Xie X, Tu TX, Zhang Y, Dai Y, Yang R, Yu ZZ (2020) Compressible, durable and conductive polydimethylsiloxane-coated MXene foams for high-performance electromagnetic interference shielding. Chem Eng J 381:122622. https://doi.org/10.1016/j.cej.2019.122622
35. Lee Y, Kim SJ, Kim YJ, Lim Y, Chae Y, Lee BJ, Kim YT, Han H, Gogotsi Y, Ahn CW (2020) Oxidation-resistant titanium carbide MXene films. J Mater Chem A 8:573–581. https://doi.org/10.1039/C9TA07036B
36. Olshtrem A, Chertopalov S, Guselnikova O, Valiev RR, Cieslar M, Miliutina E, Elashnikov R, Fitl P, Postnikov P, Lancok J, Svorcik V, Lyutakov O (2021) Plasmon-assisted MXene grafting: tuning of surface termination and stability enhancement. 2D Mater 8:045037. https://doi.org/10.1088/2053-1583/ac27c0
37. Abdolhosseinzadeh S, Schneider R, Verma A, Heier J, Nuesch F, Zhang CF (2020) Turning trash into treasure: additive free MXene sediment inks for screen-printed micro-supercapacitors. Adv Mater 32:2000716. https://doi.org/10.1002/adma.202000716
38. Alhabeb M, Maleski K, Anasori B, Lelyukh P, Clark L, Sin S, Gogotsi Y (2017) Guidelines for synthesis and processing of two-dimensional titanium carbide ($Ti_3C_2T_X$ MXene). Chem Mater 29:7633–7644. https://doi.org/10.1021/acs.chemmater.7b02847
39. Zhang CFJ, Pinilla S, McEyoy N, Cullen CP, Anasori B, Long E, Park SH, Seral-Ascaso A, Shmeliov A, Krishnan D, Morant C, Liu XH, Duesberg GS, Gogotsi Y, Nicolosi V (2017) Oxidation stability of colloidal two-dimensional titanium carbides (MXenes). Chem Mater 29:4848–4856. https://doi.org/10.1021/acs.chemmater.7b00745
40. Ma JL, Yang K, Jiang Y, Shen LX, Ma HT, Cui ZW, Du YH, Lin JB, Liu JS, Zhu N (2022) Integrating MXene waste materials into value-added products for smart wearable self-powered healthcare monitoring. Cell Rep Phys Sci 3:100908. https://doi.org/10.1016/j.xcrp.2022.100908
41. Mariano M, Mashtalir O, Antonio FQ, Ryu WH, Deng BC, Xia FN, Gogotsi Y, Taylor AD (2016) Solution-processed titanium carbide MXene films examined as highly transparent conductors. Nanoscale 8:16371–16378. https://doi.org/10.1039/C6NR03682A
42. Chen XF, Zhu YZ, Zhang M, Sui JY, Peng WC, Li Y, Zhang GL, Zhang FB, Fan XB (2019) N-butyllithium-treated $Ti_3C_2T_x$ MXene with excellent pseudocapacitor performance. ACS Nano 13:9449–9456. https://doi.org/10.1021/acsnano.9b04301
43. Ma C, Cao WT, Zhang W, Ma MG, Sun WM, Zhang J, Chen F (2021) Wearable, ultrathin and transparent bacterial celluloses/MXene film with Janus structure and excellent mechanical property for electromagnetic interference shielding. Chem Eng J 403:126438. https://doi.org/10.1016/j.cej.2020.126438
44. Pu JH, Zhao X, Zha XJ, Bai L, Ke K, Bao RY, Liu ZY, Yang MB, Yang W (2019) Multilayer structured AgNW/WPU-MXene fiber strain sensors with ultrahigh sensitivity and a wide operating range for wearable monitoring and healthcare. J Mater Chem A 7:15913–15923. https://doi.org/10.1039/C9TA04352G
45. Pandey RP, Rasheed PA, Gomez T, Azam RS, Mahmoud KA (2020) A fouling-resistant mixed-matrix nanofiltration membrane based on covalently cross-linked $Ti_3C_2T_X$ (MXene)/cellulose acetate. J Membr Sci 607:118139. https://doi.org/10.1016/j.memsci.2020.118139
46. Li YQ, Umer R, Samad YA, Zheng LX, Liao K (2013) The effect of the ultrasonication pre-treatment of graphene oxide (GO) on the mechanical properties of GO/polyvinyl alcohol composites. Carbon 55:321–327. https://doi.org/10.1016/j.carbon.2012.12.071
47. Peresin MS, Habibi Y, Zoppe JO, Pawlak JJ, Rojas OJ (2010) Nanofiber composites of polyvinyl alcohol and cellulose nanocrystals: manufacture and characterization. Biomacromolecules 11:674–681. https://doi.org/10.1021/bm901254n
48. Jin XX, Wang JF, Dai LZ, Liu XY, Li L, Yang YY, Cao YX, Wang WJ, Wu H, Guo SY (2020) Flame-retardant poly(vinyl alcohol)/MXene multilayered films with outstanding electromagnetic interference shielding and thermal conductive performances. Chem Eng J 380:122475. https://doi.org/10.1016/j.cej.2019.122475
49. Woo JH, Kim NH, Kim SI, Park OK, Lee JH (2020) Effects of the addition of boric acid on the physical properties of MXene/polyvinyl alcohol (PVA) nanocomposite. Compos B Eng 199:108205. https://doi.org/10.1016/j.compositesb.2020.108205
50. Wang W, Yuen ACY, Long H, Yang W, Li AO, Song L, Hu Y, Yeoh GH (2021) Random nano-structuring of PVA/MXene membranes for outstanding flammability resistance and electromagnetic interference shielding performances. Compos B Eng 224:109174. https://doi.org/10.1016/j.compositesb.2021.109174
51. Naguib M, Kurtoglu M, Presser V, Lu J, Niu JJ, Heon M, Hultman L, Gogotsi Y, Barsoum MW (2011) Two-dimensional nanocrystals produced by exfoliation of Ti_3AlC_2. Adv Mater 23:4248–4253. https://doi.org/10.1002/adma.201102306
52. Naguib M, Mashtalir O, Carle J, Presser V, Lu J, Hultman L, Gogotsi Y, Barsoum MW (2012) Two-dimensional transition

metal carbides. ACS Nano 6:1322–1331. https://doi.org/10.1021/nn204153h

53. Wang LB, Zhang H, Wang B, Shen CJ, Zhang CX, Hu QK, Zhou AG, Liu BZ (2016) Synthesis and electrochemical performance of $Ti_3C_2T_x$ with hydrothermal process. Electron Mater Lett 12:702–710. https://doi.org/10.1007/s13391-016-6088-z
54. Halim J, Cook KM, Naguib M, Eklund P, Gogotsi Y, Rosen J, Barsoum MW (2016) X-ray photoelectron spectroscopy of select multi-layered transition metal carbides (MXenes). Appl Surf Sci 362:406–417. https://doi.org/10.1016/j.apsusc.2015.11.089
55. Zeng ZH, Wu TT, Han DX, Ren Q, Siqueira G, Nystrom G (2020) Ultralight, flexible, and biomimetic nanocellulose/silver nanowire aerogels for electromagnetic interference shielding. ACS Nano 14:2927–2938. https://doi.org/10.1021/acsnano.9b07452
56. Usman KAS, Zhang JZ, Hegh DY, Rashed AO, Jiang DG, Lynch PA, Mota-Santiago P, Jarvis KL, Qin S, Prime EL, Naebe M, Henderson LC, Razal JM (2021) Sequentially bridged $Ti_3C_2T_x$ MXene sheets for high performance applications. Adv Mater Interfaces 8:2002043. https://doi.org/10.1002/admi.202002043
57. Gong S, Sheng XX, Li XL, Sheng MJ, Wu H, Lu X, Qu JP (2022) A multifunctional flexible composite film with excellent multi-source driven thermal management, electromagnetic interference shielding, and fire safety performance, inspired by a “brick-mortar” sandwich structure. Adv Funct Mater 32:2200570. https://doi.org/10.1002/adfm.202200570
58. Hu YQ, Hou C, Shi YX, Wu JM, Yang D, Huang ZL, Wang Y, Liu YF (2022) Freestanding $Fe_3O_4/Ti_3C_2T_x$ MXene/polyurethane composite film with efficient electromagnetic shielding and ultra-stretchable performance. Nanotechnology 33:165603. https://doi.org/10.1088/1361-6528/ac4878
59. Liu HB, Fu RL, Su XQ, Wu BY, Wang H, Xu Y, Liu XH (2021) Electrical insulating MXene/PDMS/BN composite with enhanced thermal conductivity for electromagnetic shielding application. Compos Commun 23:100593. https://doi.org/10.1016/j.coco.2020.100593
60. Hamedi MM, Hajian A, Fall AB, Hakansson K, Salajkova M, Lundell F, Wagberg L, Berglund LA (2014) Highly conducting, strong nanocomposites based on nanocellulose-assisted aqueous dispersions of single-wall carbon nanotubes. ACS Nano 8:2467–2476. https://doi.org/10.1021/nn4060368
61. Zeng ZH, Jin H, Chen MJ, Li WW, Zhou LC, Xue X, Zhang Z (2017) Microstructure design of lightweight, flexible, and high electromagnetic shielding porous multiwalled carbon nanotube/polymer composites. Small 13:1701388. https://doi.org/10.1002/smll.201701388
62. Peng MY, Qin FX (2021) Clarification of basic concepts for electromagnetic interference shielding effectiveness. J Appl Phys 130:225108. https://doi.org/10.1063/5.0075019
63. Yan DX, Pang H, Li B, Vajtai R, Xu L, Ren PG, Wang JH, Li ZM (2015) Structured reduced graphene oxide/polymer composites for ultra-efficient electromagnetic interference shielding. Adv Funct Mater 25:559–566. https://doi.org/10.1002/adfm.201403809
64. Rajavel K, Luo SB, Wan YJ, Yu XC, Hu YG, Zhu PL, Sun R, Wong CP (2020) 2D $Ti_3C_2T_x$ MXene/polyvinylidene fluoride (PVDF) nanocomposites for attenuation of electromagnetic radiation with excellent heat dissipation. Compos Part A Appl Sci Manuf 129:105693. https://doi.org/10.1016/j.compositesa.2019.105693
65. Wang Y, Qi QB, Yin G, Wang W, Yu D (2021) Flexible, ultra-light, and mechanically robust waterborne polyurethane/$Ti_3C_2T_x$ MXene/nickel ferrite hybrid aerogels for high-performance electromagnetic interference shielding. ACS Appl Mater Interfaces 13:21831–21843. https://doi.org/10.1021/acsami.1c04962
66. Sang M, Liu GH, Liu S, Wu YX, Xuan SH, Wang S, Xuan SY, Jiang WQ, Gong XL (2021) Flexible PTFE/MXene/PI soft electrothermal actuator with electromagnetic-interference shielding property. Chem Eng J 414:128883. https://doi.org/10.1016/j.cej.2021.128883
67. Wei YY, Dai ZH, Zhang YF, Zhang WW, Gu J, Hu CS, Lin XY (2022) Multifunctional waterproof MXene-coated wood with high electromagnetic shielding performance. Cellulose 29:5883–5893. https://doi.org/10.1007/s10570-022-04609-3
68. Hong SY, Sun Y, Lee J, Ma YF, Wang M, Nam JD, Suhr J (2021) 3D printing of free-standing $Ti_3C_2T_x$/PEO architecture for electromagnetic interference shielding. Polymer 236:124312. https://doi.org/10.1016/j.polymer.2021.124312
69. Miao Z, Chen XH, Zhou HL, Liu P, Fu SL, Yang JJ, Gao YH, Ren YP, Rong D (2022) Interfacing MXene flakes on a magnetic fiber network as a stretchable, flexible, electromagnetic shielding fabric. Nanomaterials 12:20. https://doi.org/10.3390/nano12010020
70. Tan CX, Dong ZG, Li YH, Zhao HG, Huang XY, Zhou ZC, Jiang JW, Long YZ, Jiang PK, Zhang TY, Sun B (2020) A high performance wearable strain sensor with advanced thermal management for motion monitoring. Nat Commun 11:3530. https://doi.org/10.1038/s41467-020-17301-6
71. Cao WT, Ma C, Mao DS, Zhang J, Ma MG, Chen F (2019) MXene-reinforced cellulose nanofibril inks for 3D-printed smart fibres and textiles. Adv Funct Mater 29:1905898. https://doi.org/10.1002/adfm.201905898
72. Lin H, Wang YW, Gao SS, Chen Y, Shi JL (2018) Theranostic 2D tantalum carbide (MXene). Adv Mater 30:1703284. https://doi.org/10.1002/adma.201703284
73. Li KR, Chang TH, Li ZP, Yang HT, Fu FF, Li TT, Ho JS, Chen PY (2019) Biomimetic MXene textures with enhanced light-to-heat conversion for solar steam generation and wearable thermal management. Adv Energy Mater 9:1901687. https://doi.org/10.1002/aenm.201901687
74. Li RY, Zhang LB, Shi L, Wang P (2017) MXene Ti_3C_2: an effective 2D light-to-heat conversion material. ACS Nano 11:3752–3759. https://doi.org/10.1021/acsnano.6b08415
75. Cao WT, Feng W, Jiang YY, Ma C, Zhou ZF, Ma MG, Chen Y, Chen F (2019) Two-dimensional MXene-reinforced robust surface superhydrophobicity with self-cleaning and photothermal-actuating binary effects. Mater Horizons 6(1057):1065. https://doi.org/10.1039/C8MH01566J